EVERGREEN - Joint Journal of Novel Carbon Resource Sciences & Green Asia Strategy, Vol. 13, Issue 01, pp. 200-211, March, 2026

Experimental Analysis of L-Shaped Oscillating Water Column with Horizontal Chamber Length Variations under Different Wave Periods

Destyariani Liana Putri[1,*], Luh Putri Adnyani[1], Nurmawati[1],
Muhammad Khaisar Wirawan[1], Diniar Mungil Kurniawati[2],
Malik Kharim[1], Jawahir Al Kalamul Haq[3], Adnan Sandy Dwi Marta[1,4,*]

[1]Ocean Engineering Study Program, Institut Teknologi Kalimantan, Balikpapan, Indonesia
[2]Mechanical Engineering Study Program, Institut Teknologi Kalimantan, Balikpapan, Indonesia
[3]Directorate of Laboratory Management, Research Facilities, and Science and Technology Park, National Research and Innovation Agency, BRIN, Tangerang, 15314, Indonesia
[4]Research Center for Hydrodynamics Technology, National Research and Innovation Agency, BRIN, Surabaya, 60112, Indonesia

*Author to whom correspondence should be addressed:
E-mail: putridestyariani@lecturer.itk.ac.id; adna001@brin.go.id

(Received May 28, 2025; Revised September 10, 2025; Accepted December 16, 2025)

Abstract: Wave power plants using the oscillating water column (OWC) type have been implemented at full scale, with chamber geometry design variations (L-shaped OWC chamber) and including various wave periods test. The experimental study was conducted on 1:10 scale model in a glass flume (1 x 1.5 x 35) meters at the Coastal Engineering Laboratory of the National Research and Innovation Agency (BRIN). The objective is to investigate the effects of wave period and height variations on the power output of the L-OWC device, including the influence of L-OWC chamber length variations on water surface oscillation, pneumatic pressure, and air velocity in the chamber and turbine duct. The findings highlight that the input water level oscillation and period significantly impact the power output generated by the device. The water level oscillation changes in the L-OWC chamber's geometry length, affects water surface oscillation, pressure, and air velocity in the chamber and turbine duct. The highest power output was achieved with the L1 geometry rather than L2 during the test when the air was entering the chamber, generating a power output of 49.99 W and 46.91 W respectively.

Keywords: chamber geometry; chamber length variations; L-OWC; Oscillating Water Column; wave flume experiment; wave period variation

1. Introduction

A growing amount of attention has been paid in recent years to phenomena that have socioeconomic and geopolitical ramifications, specifically energy transformation brought about by the growth of alternative energy1). Renewable energy has emerged as a substitute for fossil fuels as a source of electrical energy.A key component of monetary development is energy2). Global energy demand has increased as a result of economic growth. Numerous researchers work to enhance and develop well-known energy sources3). Ocean energy, particularly wave energy, is acknowledged as a renewable energy source with significant potential to fulfil world energy requirements. The Oscillating Water Column (OWC) technology has garnered interest due to its straightforward design and extensive applicability in coastal regions4). Recent research and advancements have demonstrated enhancements in the efficiency and stability of OWC systems, applicable to both fixed and floating converters.

The shape of the chamber utilised is a primary factor influencing the efficacy of OWC. The chamber's geometry influences the dynamic response of the water within, subsequently determining the pressure and velocity of the resultant airflow5),6). Recent studies indicate that design modifications, including multi-chamber configurations and oblique shapes, exhibit substantial variances in OWC performance 7),8). The L-shape of the OWC chamber (L-OWC) provides a distinctive form that enhances the regulation of water dynamics within the chamber,

Cite: D. Putri et al., "Experimental Analysis of L-Shaped Oscillating Water Column with Horizontal Chamber Length Variations under Different Wave Periods". Evergreen, 13 (01) 200-211 (2026). https://doi.org/10.5109/7407645.

particularly under specific wave circumstances 9,10). Nonetheless, the impact of this configuration on hydrodynamic response and performance necessitates further elucidation using experimental methodologies.

However, wave factors like wave period have a big impact on L-OWC efficiency because they change the way the water inside the chamber oscillates, which in turn affects the pressure and air flow that result8,9). Recent studies indicate that waves with extended periods enhance the oscillation amplitude and pressure within the chamber, hence optimising the power output of the OWC. Initially the 1,452 mm L-shaped OWC generated 337 W and the 1,388 mm L-shaped generated smaller power output in 80 W where they were equally tested in 1:10 laboratory scale 10-14). Experimental testing have demonstrated that fluctuations in wave period15,16), can influence the thermodynamic response within the chamber, which is crucial for commercial applications17). Despite numerous studies on the influence of wave period on OWC, additional research is essential, particularly for the design of L-OWC under fluctuating wave conditions.

The previous research also shows the output that greater wave periods scenario achieved better performance which 7,089 RPM at 7.5 s and 5,190 RPM at 11.5 s 18). Hence, this study seeks to address this gap by examining the impact of variations in horizontal chamber length on the L-OWC system in relation to changes in wave period. This study will utilise an experimental method in a wave test channel to ascertain the impact of L-OWC geometric variations on chamber oscillations, pressure profiles, and airflow velocity. This study aims to enhance understanding of OWC design optimisation and serves as an initial step towards developing a more efficient renewable energy system in coastal areas.

2. Methodology

2.1. Experimental Setup

The experiment was performed in a laboratory flume of 1 meter in width, 1.5 meters in height, and 36 meters in length. A piston-type wavemaker generated waves with regulated properties[19]. The spacing and model configuration in the flume adhered to the Hydralab III guidelines to guarantee wave stability and reduce reflection effects prior to the waves encountering the L-OWC structure[20].

The resulting regular waves adhere to the Airy wave theory[11], showing period variations ranging from 6.5 seconds to 14.5 seconds and wave height variations reaching up to 2.25 meters[21]. The tests were performed at a scale of 1:10, adhering to the Froude scaling law to align laboratory conditions with field conditions[22]. The scaling ensures geometric similarity between model and prototype dimensions. In addition, kinematic similarity was maintained by ensuring the correct wave celerity and fluid particle trajectories under scaled wave conditions. Furthermore, dynamic similarity was achieved by matching the Froude number between model and prototype, preserving the ratio of inertial to gravitational forces. The scalability is crucial for preserving the fluid dynamics correspondence between the small-scale model and the field prototype, facilitating the extrapolation of laboratory results to the prototype scale while considering dynamic similarities [18],[23].

An L-shaped OWC with two variations of horizontal column lengths was tested to analyze the effect of geometry on chamber oscillations, pressure distribution, and airflow velocity. The choice of this shape and variation was informed by prior research demonstrating a significant impact of geometry on energy conversion efficiency in OWC systems[24,25].

2.2. Sensor Configuration and Data Acquisition

The seven wave gauges are employed to assess wave height and interaction parameters. One wave gauge is positioned 1 (one) meter in front of the wavemaker for initial measurement. Four wave gauges are positioned in front of the L-OWC structure to compute the reflection coefficient utilization[26,27]. Two wave gauges are positioned within the L-OWC chamber to assess internal oscillations and validate oscillation data.

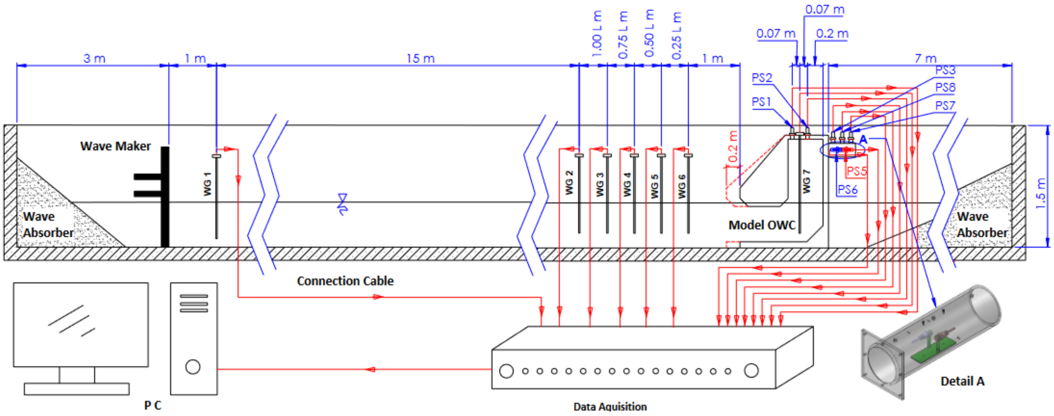

Fig. 1: Flume Laboratory Modes of Operation

Cite: D. Putri et al., "Experimental Analysis of L-Shaped Oscillating Water Column with Horizontal Chamber Length Variations under Different Wave Periods". Evergreen, 13 (01) 200-211 (2026). https://doi.org/10.5109/7407645.

The seven pressure gauges are employed to quantify pressure. Two pressure gauges in the chamber to measure pressure variations in the oscillating water column. Five pressure gauges (PGs) are located in the turbine duct: one for static pressure (P_s) measured by sensor PG8, two for total pressure (P_t) in the outflow direction measured by sensor PG5, and one for total pressure from the inflow measured by sensor PG6 to assess air pressure decompression[28)].

Furthermore, PG3 and PG7 are utilised to acquire the pressure distribution within the turbine duct (refer to Figure 1). These sensors are utilised to quantify air velocity via the Bernoulli equation[29)]. The sample rates employed in this experiment are 40 Hz, to mitigate the impacts of scaling. Furthermore, all sensor devices have been calibrated in accordance with ISO 17025 standards[30)].

To ensure accurate data acquisition, all measurement instruments were calibrated prior to testing. The wave gauges (WG) used in this study were resistive-type sensors with a measurement accuracy of ±0.5 mm. Meanwhile, the pressure gauges (PG) were piezoresistive flush-face-type sensors with an accuracy of ±0.5% of the full-scale range. Each sensor underwent linear calibration procedures using controlled input signals. The calibration results showed excellent linearity for both WG and PG, with coefficients of determination (R^2) ranging from 0.9995 to 0.9999, indicating a high level of precision and reliability. Figure 1 example of calibration curves of Pressure Gauge (PG1) and Wave Gauge (WG1); all instruments in this study show similar high R^2 values (see Table 1).

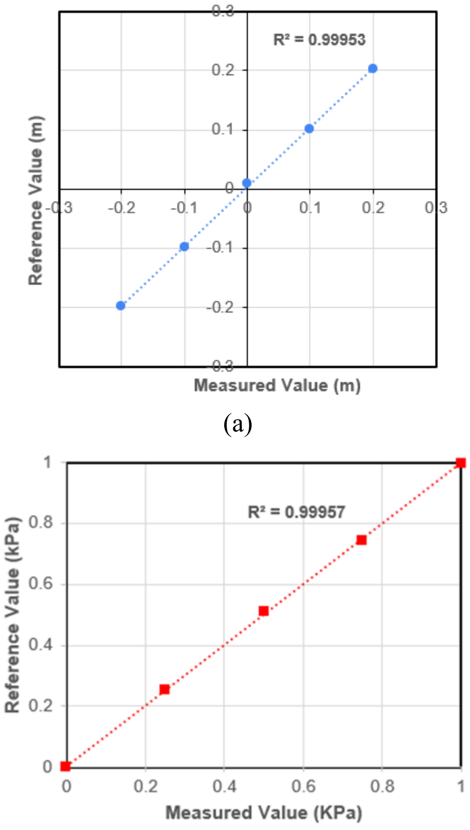

(a)

(b)

Fig. 2: Calibration curves of Pressure Gauge (PG1) and Wave Gauge (WG1) with corresponding R^2 values

Table 1: Calibration Results of Pressure and Wave Gauges

PG	R² - PG	WG	R² - WG
PG 1	0.99953	WG 1	0.99957
PG 2	0.99953	WG 2	0.99993
PG 3	0.99953	WG 3	0.99992
PG 4	0.99953	WG 4	0.99993
PG 5	0.99998	WG 5	0.99992
PG 6	0.99998	WG 6	0.99991
PG 7	0.99998	WG 7	0.99884
PG 8	0.99998	WG 8	0.99896

The uncertainty of the generated power output was estimated using the uncertainty propagation method described by Taylor (1996). For a derived quantity $q=f(x_1, x_2,\ldots,x_n)$, the combined uncertainty Δq is computed using the root-sum-square of the partial derivatives of each input variable, as follows:

$$\Delta q = \sqrt{\begin{array}{c}(\frac{\partial q}{\partial x_1}.\Delta x_1)^2 + (\frac{\partial q}{\partial x_1}.\Delta x_2)^2 + \ldots \\ +(\frac{\partial q}{\partial x_1}.\Delta x_n)^2\end{array}} \qquad (1)$$

By applying this approach to the wave power calculation defined in Equation (1), which incorporates measured parameters such as wave height, wave period, and dynamic pressure obtained from pressure gauges installed in the turbine duct, the overall uncertainty in the experimental power output was determined to be ±0.711%. This relative uncertainty reflects the combined influence of instrumental precision and measurement variability, offering a reliable confidence level in the assessment of wave energy conversion performance.

2.3. Experimental Procedure

Testing was conducted with wave generation periods varying from 60 to 120 seconds in accordance with Ocean Energy Systems (OES) guidelines[31)] and the Wave Energy Handbook[21)] to ensure stable data. The distance between the wavemaker and the structure was in accordance with the Hydralab III guidelines to reduce the effects of secondary wave disturbances before reaching the L-OWC structure. In Figure 3, Geo 1 refers to the L-OWC with a shorter horizontal chamber, indicated by the blue line, while Geo 2 represents the L-OWC with a longer horizontal chamber, shown with the red line.

In this study, the experimental model (Table 2) was designed using the Froude scaling law with a scale factor of 1:10 to ensure similarity between the laboratory model

Table 2: Experimental Testing Conditions

Parameter	Variables
Wave Generation (Test scenario)	H (m) and T (s) T (s) = 2.06; 2.37; 2.69; 3.0; 3.32; 3.64; 3.95; 4.27; 4.59; with the H (m) = 0.225*
Geometry (length of horizontal columns)	Geometry 1 (Geo 1) and Geometry 2 (Geo 2)** Turbine duct = 0.16 m
Others	Water depth (d) = 0.75 m Regular Wave

** Parameters and variables are scaled to a 1:10 model scale using the Froude scaling law*
*** See Figure 3*
Notes: Length – wave height (m) = k; Time – wave period (s) = $k^{1/2}$

and the prototype in real sea conditions. The scaling process considered not only the geometric dimensions of the L-OWC chamber, but also the wave generation parameters (wave height, wave period) and other hydrodynamic factors. Geometric similarity was maintained by proportionally reducing all linear dimensions of the prototype (chamber length, duct size, and water depth) by a factor of 10. For example, the actual turbine duct of 1.6 m was scaled to 0.16 m in the model, and the water depth of 7.5 m was represented as 0.75 m in the flume.

In addition, kinematic similarity was ensured by scaling the wave period (T) using the square root of the scale factor ($\lambda^{0.5}$). For instance, a prototype wave period of approximately 6.5–14.5 s corresponds to the experimental wave period range of 2.06–4.59 s in the model. Likewise, the prototype wave height of 2.25 m was represented as 0.225 m in the flume.

Dynamic similarity was governed by equating the Froude number between the model and the prototype, which ensures that the ratio of inertial to gravitational forces is consistent. This approach is suitable for free-surface hydrodynamics such as wave–structure interaction problems. Reynolds number similarity could not be fully achieved due to viscosity scaling, but since wave energy devices are dominated by gravitational and inertial forces, Froude scaling is considered valid. Through these scaling steps, the experimental conditions accurately represent the hydrodynamic behaviour of the L-OWC chamber in real sea conditions. The process ensures that wave–structure interactions, chamber oscillations, and turbine duct responses in the model test are dynamically comparable to those expected at full scale.

The hydrodynamic performances of OWC are expressed using non-dimensional hydrodynamic parameters (See Table 2), which are covered in this section [12,32]. The ratio of the incident wave height (H) to the maximum variation of free surface elevation (fse_{max}) within the chamber is known as the wave amplification factor (WAF)[33,34].

$$WAF = \frac{fse_{max}}{H} \tag{2}$$

Because of the oscillation of the water column, the non-dimensional air pressure inside the OWC (AP) chamber can be calculated as

$$AP = \frac{(P_{air})}{H} \tag{3}$$

The efficacy of the L-OWC system in wave energy conversion is analysed by recording the pressure and wave height data in real time and subsequently processing it. Bernoulli's equation is used to calculate the air velocity in the duct based on the total of pressure difference (P_t) and statical pressure (P_s)[35]:

$$v_{duct} = \frac{\sqrt{2(P_t - P_s)}}{\rho} \tag{4}$$

where v_{duct} is air velocity and ρ adalah air density. The power input within the duct of an OWC-type wave energy turbine is affected by both the airflow rate and the incoming airflow velocity into the turbine. This input

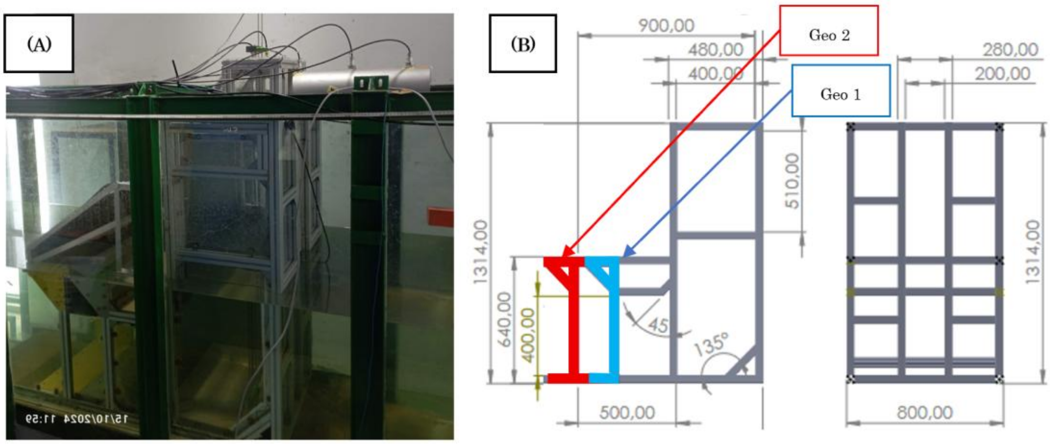

Fig. 3: L-OWC chamber :(A) model test in flume; (B) detail geometry (in milimeters)

Cite: D. Putri et al., "Experimental Analysis of L-Shaped Oscillating Water Column with Horizontal Chamber Length Variations under Different Wave Periods". Evergreen, 13 (01) 200-211 (2026). https://doi.org/10.5109/7407645.

power is expressed as follows [11]:

$$P_{OWC} = \frac{1}{2}\,\rho.A.v^3 \tag{5}$$

In equation (5), Where P_{owc} represents the power generated within the turbine duct, A is the cross-sectional area of the turbine duct, and v_{duct} is the airflow velocity entering and exiting the turbine duct.

3. Results and Discussion

3.1. Characteristic of Free Surface Elevation (fse) and Air Pressure (Pair) di chamber L-OWC

The correlation between water level oscillation - $WG_{chamber}$ (orange line) and air pressure - $PG_{chamber}$ (dashed green line) exemplifies the principal phenomenon in the Oscillating Water Column (OWC), wherein water oscillation induces air pressure that is harnessed for energy generation. Figure 4 illustrates the distinctive timeseries graph of fse and P_{air}, using timeseries samples at T_{in} = 2.06 s, 3.32 s, and 4.59 s. T_{in} = 2.06 s represents the shortest wave period generated in the test scenario, T_{in} = 3.32 s corresponds to a medium wave period, and T_{in} = 4.59 s signifies the greatest wave period generated in the scenario. Wave oscillation and air pressure in the chamber exhibit distinct features based on T_{in}.

The oscillation amplitude in $WG_{chamber}$ exceeds that of WG_{in}, indicating wave amplification within the chamber. At T_{in} = 2.06 s, the wave oscillation pattern entering the chamber exhibits regularity and amplifies in accordance with the generation wave pattern; this feature is also consistent with the P_{air} pattern characteristic (see Figure 4). The oscillation properties of the wave in the chamber depicted by $WG_{chamber}$ at T_{in} = 3.32 s and T_{in} = 4.59 s exhibit a distinct pattern compared to WG_{in}. At 3.32 s and 4.59 s, the wave oscillation entering the chamber seems to

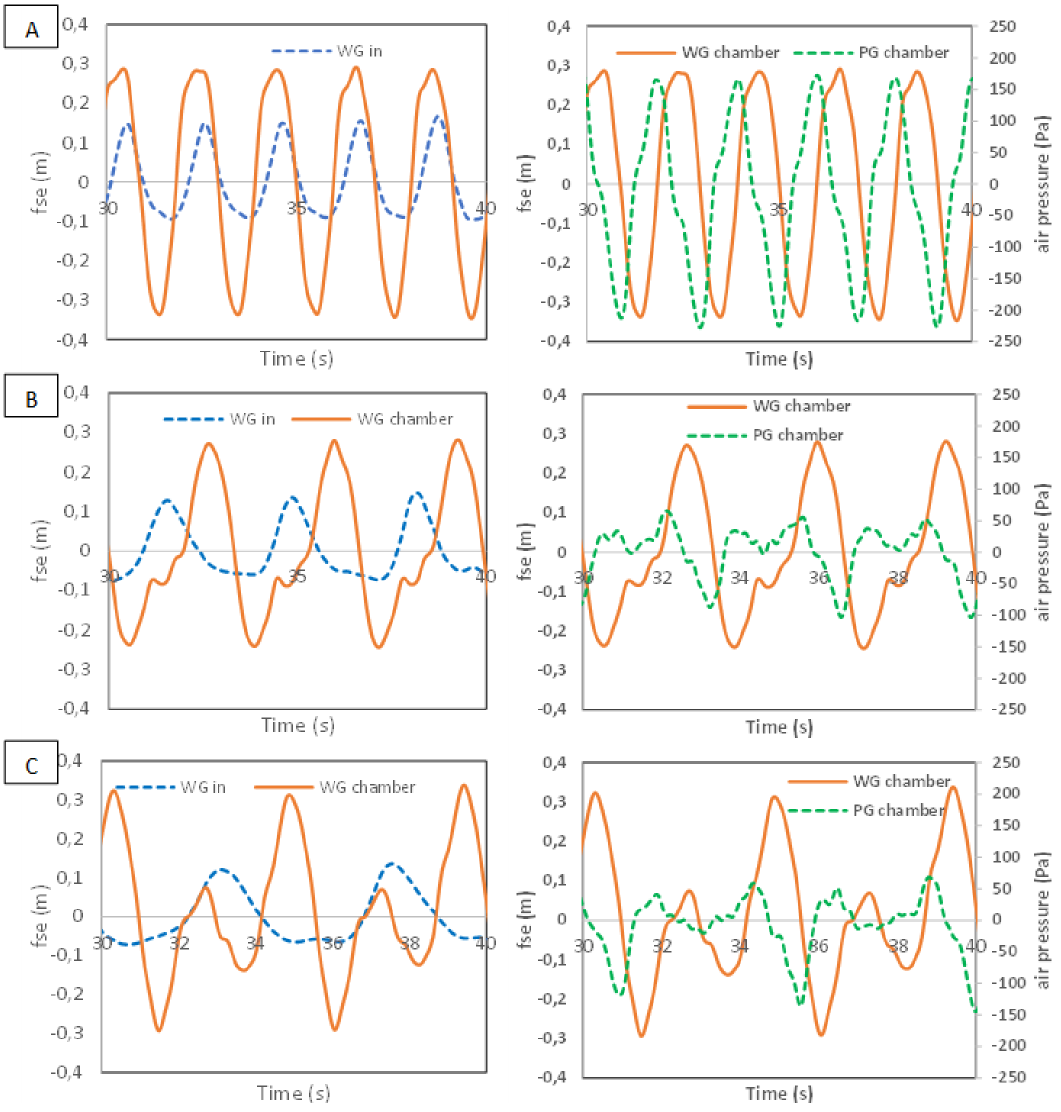

Fig. 4: Time series for free surface elevation (fse) oscillations in wave generation and chamber, as well as the air pressure in the chamber in the wave generation scenario 0.225 m, (a) T_{in}= 2.06 s; (b) T_{in}= 3.32 s; (c) T_{in}= 4.59 s of Geometry 1

be wave modulated, and wave distortion is evident even at $PG_{chamber}$ (see to Figures 3b and 3c). The amplitude of air pressure oscillations seems to be more attenuated than that of water level oscillations. This may arise from energy dissipation within the system, as observed in the test case $T_{in} = 3.32$ s.

3.2. The Effect of Pneumatic Air Pressure on Airflow Velocity

Figure 5 illustrates the attributes of total compression pressure (PT_{out}), total decompression pressure (PT_{in}), and static pressure (PS) at $H_{in} = 0.025$ m and $T_{in} = 2.06$ s (see Figure 1). The disparity in total compression pressure is indicated by the red dashed line, while total decompression pressure is represented by the green dashed line. The disparity between PT_{out} and PT_{in} with PS constitutes the dynamic pressure (Pd), which is transformed into air velocity (v) within the turbine duct (Equation 2). The graph indicates that at the peak phase (positive pressure), the differential between PT_{out} and PS generates dynamic pressure, facilitating air egress from the chamber. Nevertheless, the magnitude of this change is comparatively lesser than that of decompression (PT_{in} vs PS at the wave trough). The greater amplitude of PT_{out} relative to PS signifies the efficacy of air output, despite the intensity being lower than during the decompression phase.

Decompression produces a greater value than compression, as evidenced by the substantial disparity between PT_{in} and PS during the valley period (negative pressure). This signifies that the air entering the chamber is more prevalent. This signifies that the air oscillation within the chamber is predominantly influenced by the inflow phase rather than the outflow. The greater decompression relative to compression signifies that the system is more adept at intake than expulsion of air. This may result from the chamber geometry design that facilitates air input and the wave effect that enhances negative pressure production. This pressure fluctuation suggests that the chamber geometry design is more orientated towards optimising decompression rather than compression.

3.3. Correlation between Water Level Oscillation (*fse*) and Air Pressure in The Chamber

The air pressure in the chambers of Geo 1 and Geo is directly associated with the amplitude of the water level oscillation (*fse*). As the water level rises, air pressure often increases; conversely, as the water level falls, air pressure generally reduces. Each wave period exhibits a variable pressure pattern, signifying the existence of pressure dynamics resulting from the interaction of water waves within the chamber. The air pressure in Geo 1 (blue line) generally exceeds that of Geo 2 (orange line) throughout the majority of water level fluctuations. This suggests that the geometric configuration of Geo 1 is preferable in generating higher air pressure compared to Geo 2.

In Figure 6, Geo 2 has a reduced wave period ($Tin \leq 3.0$ s), with air pressure demonstrating more pronounced variations and a progressive decline (Refer to Figure 4). At extended wave periods ($Tin \geq 4.7$ s), the pressure amplitude exhibits an increase, suggesting a resonance effect or dynamic equilibrium between the water surface and the chamber. The total pressure in the chamber at $2.06 \text{ s} \leq Tin \leq 3.00$ s, which exhibits a higher value, signifies a more robust air pressure response, potentially attributable to its superior design in harnessing energy from water surface oscillations. At $3.00 \text{ s} \leq Tin < 3.95$ s, the chamber exhibits a reduced air pressure value, suggesting a diminished air pressure pattern, which may imply less efficiency in harnessing oscillation energy.

In Figure 7 (a), the air pressure within the chamber decreases as the wave period extends from Tin = 2.06 s to Tin = 3.64 s, ultimately attaining a minimum value of 63.90 Pa. Following the wave period T = 3.64 s, the pressure rises once more, reaching a second high value at Tin = 4.27 s of 237.00 Pa. A like trend is observed in Geo

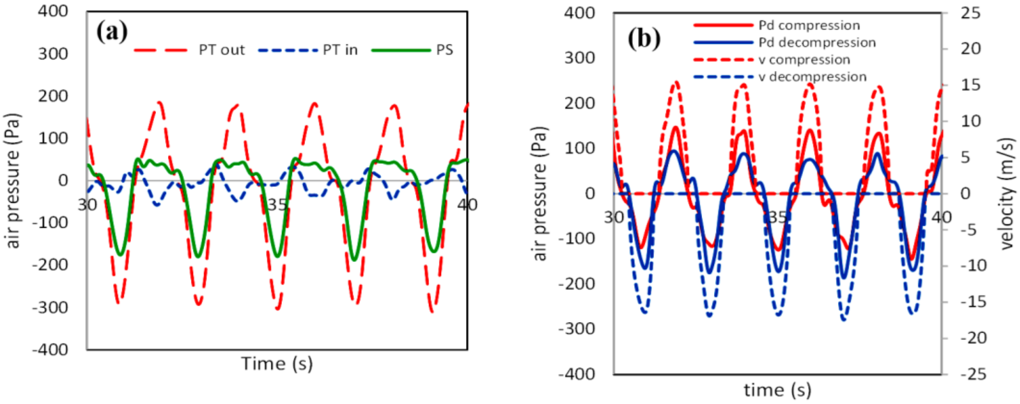

Fig. 5: Turbine Duct Characteristics and Patterns of Geometry 1 in The Test Scenario Hin= 0.225 m, Tin=2.06 s, (a) Total Air Pressure and Static, (b) Dynamic Pressure and Velocity

2, where the pressure diminishes from Tin = 2.06 s to Tin = 3.64 s, attaining a minimum value of 56.43 Pa (see Figure 7 (b)). The air pressure rises once more after Tin = 3.64 s, reaching a second peak value of 191.53 Pa at Tin = 4.27 s. At all wave times, the air pressure in Geo 1 exceeds that of Geo 2, except at Tin = 2.37 s, where Geo 2 exhibits a greater pressure (381.77 Pa) than Geo 1 (315.33 Pa). During short wave periods (Tin ≤ 2.37 s), both air pressure and water level fluctuations exhibit peak values, potentially indicating resonance with the chamber's design. At extended wave periods (Tin ≥ 3.64 s), a resurgence of air pressure follows a decline, signifying the impact of resonance dynamics between waves and geometry.

3.4. Correlation between Water Level Oscillation (fse) in the Chamber and Airflow Velocity in the Turbine Duct

In Figure 8, In Geo 1 (red dashed line), the airflow velocity in the turbine duct exhibits a gradual decline during compression as the wave period extends from Tin = 2.376 s to Tin = 3.95 s, followed by a further increase from Tin = 4.27 s to Tin = 4.59 s. During decompression (blue dashed line), the velocity within the turbine duct exceeds that of the compression phase. Nonetheless, the general trend resembles the compression pattern. In Geo 2, the compression (red solid line) exhibits a worse velocity performance compared to Geo 1 across nearly the entire frequency spectrum. This signifies that the geometry is suboptimal for compressing airflow into the turbine duct.

During the decompression phenomena (blue solid line), the velocity within the turbine duct markedly escalates at Tin = 4.27 s. Figure 8 indicates that the decompression airflow velocity values in nearly all wave period scenarios of Generation and Geometry exceed those seen during compression. In Geo 1 and Geo 2, the decompression airflow velocity is significantly greater than that of the compression flow. This indicates that the two geometries are appropriate for converting energy from the airflow into the chamber.

Both compression and decompression phases contribute significantly to the overall performance of the OWC system, as the bidirectional airflow directly affects the energy input to the turbine. However, in this L-OWC experimental setup, the decompression phase is more dominant than compression, as shown in Figure 8, indicating a greater potential for energy conversion during the decompression cycle.

In Figure 9 (a), the airflow velocity (v) in Geo 1 decreases with an increasing wave period until Tin = 3.64 s, after which it exhibits a minor rise for larger periods Tin = 4.27 s and 4.59 s. The oscillation of the water level (fse) exhibits a non-linear fluctuation, peaking at Tin = 2.37 s (0.69 m), and experiencing a substantial decline at Tin = 3.64 s (0.34 m). In Geo 2, the airflow velocity (v) exhibits a comparable trend; however, Geo 2 consistently has a greater v value than Geo 1 during the majority of wave periods. The oscillation of water levels (fse) in Geo 2 is somewhat lower than in Geo 1 during short intervals (Tin = 2.06 s to 2.69 s), although exhibits greater stability in medium to long periods. Overall, Geo 2 has a superior v value relative to Geo 1, particularly at Tin = 2.37 s (Geo 2: 15.96 m/s, Geo 1: 14.45 m/s) and Tin = 4.59 s (Geo 2: 12.30 m/s, Geo 1: 11.88 m/s).

There is a positive correlation between fse and v, when the water level oscillation in the chamber is larger (high fse), the airflow velocity in the turbine duct tends to increase. Nonetheless, the efficacy of energy transfer from fse to v is superior in Geo 2 (see Figure (b)). This may result from

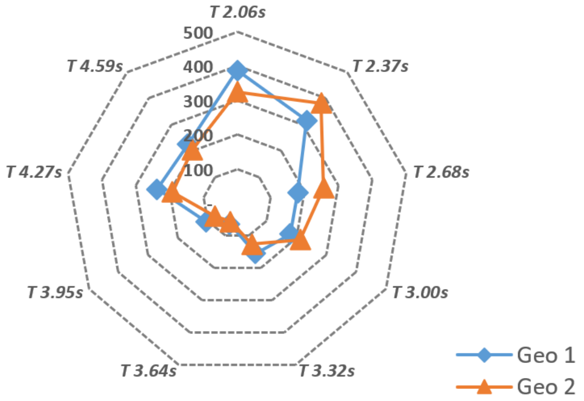

Fig. 6: Air Pressure Correlation in Chamber due to Wave Period Variations

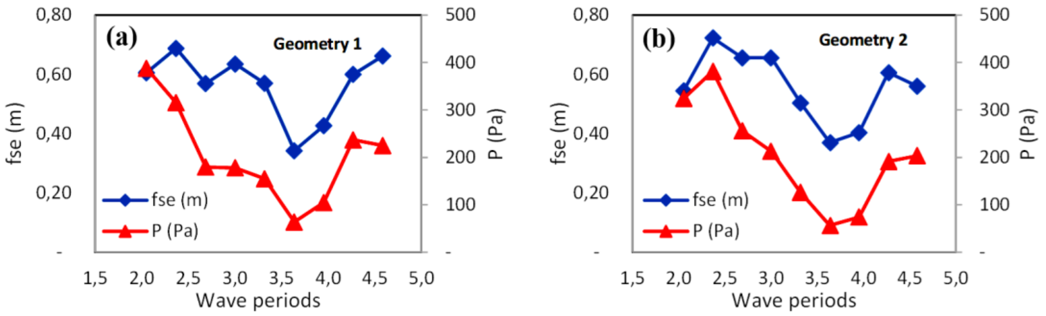

Fig. 7: The Effect of Water Level Oscillations in the Chamber on Airflow Velocity in Turbine Duct, (a) Geometry 1, (b) Geometry 2

its superior geometric design in transforming wave energy into airflow. During a brief period of T_{in} = 2.06–2.69 s, Geo 1 and Geo 2 generate elevated airflow velocities, with Geo 2 demonstrating superior efficiency. The oscillation of the water level (fse) is notably elevated during this interval, signifying an optimal reaction to small waves. During medium periods (T_{in} = 3.00–3.64 s), the v values in both geometries diminish, with Geo 1 exhibiting a more pronounced decline. In Figures 8 (a) and (b), the reduction in fse in Geo 1 surpasses that in Geo 2, suggesting that Geo 2 exhibits stronger stability in response to medium waves. During an extended period (T_{in} = 3.95–4.59 s), the airflow velocity experiences an increase once more, particularly in Geo 2. Geo 2 surpasses Geo 1 in generating consistent airflow velocity.

3.5. Non Dimensional Analysis and The L-OWC Power Generated

The d/L value (the ratio of water depth to wavelength) is inversely related to wavelength; thus, the Wave Amplification Factor (*WAF*) pattern illustrates the impact of varying wavelength on wave amplification in both geometries (refer to Figure 10 (a)). The WAF generally reaches its maximum at conditions around the resonance of the OWC system, subsequently decreasing at lower d/L ratios. A comparison of the WAF values for the two geometries will determine which is more effective at amplifying waves under varying d/L circumstances. In all geometries (Geo 1 and Geo 2), the Wave Amplification Factor (WAF) exhibits an initial increase until it attains a maximum, subsequently declining as d/L diminishes. At low d/L levels < 0.08, the WAF diminishes markedly, presumably due to decreased wave resonance efficacy (refer to Figure 10 (a)).

Geo 1 attains a peak WAF value of 3.06 at d/L=0.128, but Geo 2 achieves a somewhat superior maximum WAF of 3.21 at the same d/L, suggesting that Geo 2 exhibits greater efficacy under specific resonance settings. In Figure 10 (a), Geo 2 exhibits a superior WAF compared to Geo 1 across the majority of d/L values, particularly around the maximum value. At lesser d/L values below 0.072, the disparity between Geo 1 and Geo 2 diminishes, suggesting that the influence of geometric design is more pronounced at medium to high d/L ratios. The graph indicates that optimal resonance is achieved at a d/L ratio of approximately 0.128, where wave energy is most effectively harnessed by the OWC chamber. As the d/L value diminishes, the wave energy available for amplification diminishes, leading to a reduced WAF.

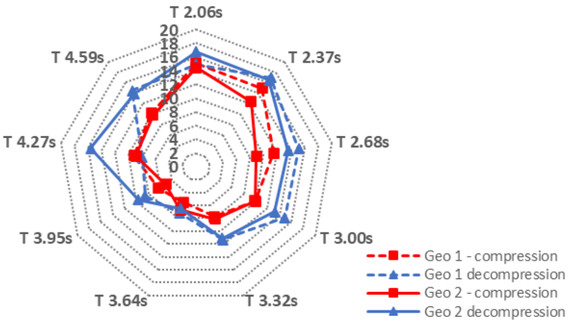

Fig. 8: Characteristics of Compression and Decompression Airflow Velocity

In Figure 10 (b), the AP value often decreases concomitantly with the reduction in the (d/L) value. The primary peaks for AP in Geo 1 and Geo 2 occur at d/L = 0.152, where the AP in Geo 1 reaches a maximum value of 0.142. In Geo 2, the amplitude of the AP reaches its peak at d/L = 0.129, with a value of 0.140. At elevated d/L (> 0.1), Geo 1 has a greater AP value than Geo 2. At reduced d/L (< 0.1), Geo 2 exhibits a more stable AP and nearly aligns with Geo 1 (refer to Figure 10 (b)). Geo 1 and Geo 2 exhibit a comparable trend, characterised by an increase in AP from low d/L to a maximum, followed by a substantial decline at a reduced (d/L). Geo 2 exhibits a superior AP at d/L = 0.128, demonstrating the efficacy of resonance in this design under these conditions.

The elevated AP values for d/L = 0.152 and 0.123 indicate the best conditions for Geo 1 and Geo 2 in harnessing wave energy. This suggests that the d/L values facilitate the maximal oscillation of the water column. This may result from design variations that influence the efficacy of wave energy transmission to air pressure. In Figure 10, the low d/L ratio of less than 0.08 results in a significant decrease in the AP value for both geometries. This suggests that the water depth is insufficient to generate substantial air

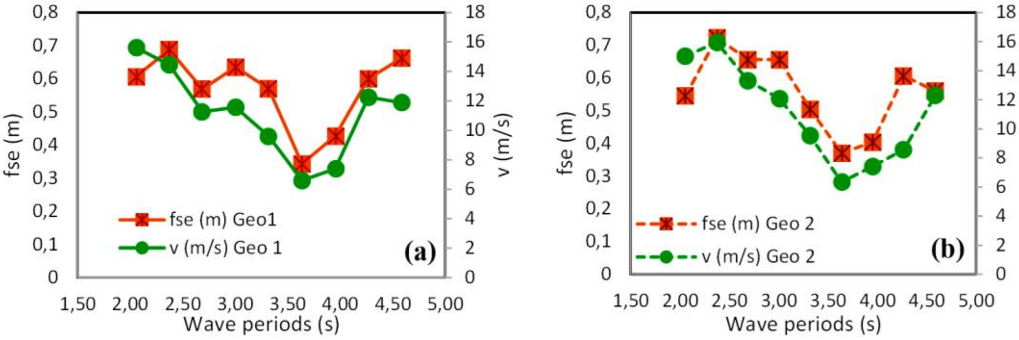

Fig. 9: Correlation of Free surface elevation (fse) in the chamber to airflow velocity, (a) Geometry 1; (b) Geometry 2

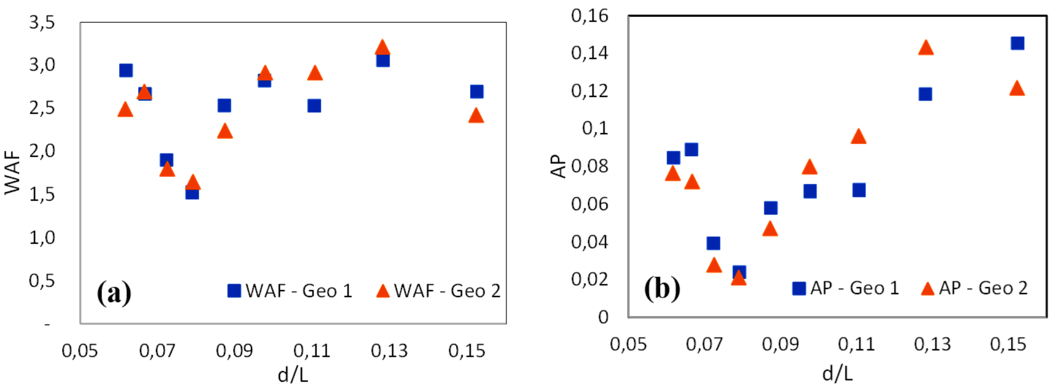

Fig. 10: Correlation of Wave Amplification Factor, Inside Air Pressure with d/L, (a) WAF vs d/L; (b) AP vs d/L

pressure. Geo 2 may possess a superior design for wave capture at specific depths, particularly within the range of 0.1 < d/L < 0.15.

Optimisation of geometric design may be necessary to enhance efficiency at low d/L ratios. The AP values for both geometries generally diminish when d/L values decline from 0.15 to approximately 0.08. Nevertheless, subsequent to the minimal point at approximately d/L = 0.08, the AP begins to rise once more. The minimum value of AP is seen at around d/L = 0.08 for both geometries. Currently, the efficacy of water column oscillations in producing air pressure may be diminished. At lower values of d/L <0.08, the pressure rises once again, potentially attributable to more intricate wave interactions within the oscillation chamber.

The performance differences between Geo 1 and Geo 2 in terms of WAF and AP (Figure 10) indicate that no single geometry consistently outperforms the other across all d/L conditions. This is due to the complex interaction between geometry shape, wave resonance, and d/L, which influences the hydrodynamic response of the chamber. Geo 2 performs optimally around d/L = 0.128–0.129, while Geo 1 reaches its peak at d/L = 0.152. The crossing of the curves suggests that the superiority of a geometry depends strongly on local wave conditions and is not absolute.

The crossing behavior of WAF and AP between Geo 1 and Geo 2 (Figure 10) is explained by the difference in chamber lengths, which alters the natural resonance frequency of each OWC geometry (See Figure 11). Geo 1 reaches its peak response at a slightly longer wave period (d/L ≈ 0.152), while Geo 2 resonates more effectively at a shorter period (d/L ≈ 0.128–0.129). This indicates that the choice of geometry should be aligned with the probability distribution of wave periods at the target location. If the prevailing sea states correspond to longer periods, Geo 1 would be more advantageous, whereas Geo 2 is superior for shorter periods. This interpretation is consistent with the findings of Rezanejad et al. (2017), López et al. (2021) and Marta et al. (2024)$^{9),12),14}$, who reported that OWC chamber performance is highly dependent on geometry-induced resonance characteristics and the dominant wave conditions at the site.

Fig. 11: Flow Visualization in the L-OWC Chamber

Cite: D. Putri et al., "Experimental Analysis of L-Shaped Oscillating Water Column with Horizontal Chamber Length Variations under Different Wave Periods". Evergreen, 13 (01) 200-211 (2026). https://doi.org/10.5109/7407645.

The power calculation depicted in Figure 10 is articulated by equation (5), representing the power within the turbine duct. In Figure 12, the power decreases as d/L diminishes until it attains a minimum at approximately d/L = 0.079, after which it increases again for lesser d/L values (below 0.072). On Geo 1, the maximum power recorded was 46.91 W at d/L = 0.152, while the minimum power was 3.53 W at d/L = 0.079. On Geo 2, the maximum power recorded was 49.99 W at d/L = 0.128, whilst the minimum power was 3.15 W at d/L = 0.079. At a greater d/L value (0.152 compared to 0.111), Geo 1 exhibits superior power relative to Geo 2, with outputs of 46.91 W versus 41.51 W at d/L = 0.152. In the meantime, Geo 2 demonstrates superiority at d/L = 0.128 (49.99 W compared to 37.15 W) and d/L = 0.111 (29.07 W compared to 17.55 W). At lower d/L values (below 0.087), the power output of Geo 1 and Geo 2 is comparatively similar, except at d/L = 0.067, where Geo 1 exceeds Geo 2 (22.62 W vs 7.76 W). At d/L = 0.062, Geo 2 exhibits marginal superiority (22.91 W compared to 20.66 W).

Geo 1 has greater efficiency for bigger d/L values (0.152 and 0.098–0.087), likely due to its geometric configuration being more conducive to optimising wave-chamber interaction at those depths. Conversely, Geo 2 has superior performance at d/L = 0.128 and 0.111, signifying enhanced adaptability to marginally longer waves. At tiny d/L (<0.079), the power thereafter increases. This may result from partial resonance circumstances, despite the overall power being low. Geo 1's performance excels at high d/L ratios, but Geo 2 is more effective under moderate d/L settings. The reduction in power at d/L = 0.079 signifies a minimum efficiency zone inside the system, potentially attributable to predominant energy dissipation. The augmentation of power at tiny d/L (<0.072) may suggest the occurrence of partial resonance phenomena or heightened oscillations that commence to harness wave energy more efficiently. This combination warrants more analysis, particularly to enhance the geometric design for diverse d/L circumstances. Geo 1 and Geo 2 each demonstrate strengths at different wave periods, highlighting that performance is not absolute but wave-dependent. This emphasizes the importance of selecting a chamber design that matches the dominant wave characteristics at the target location.

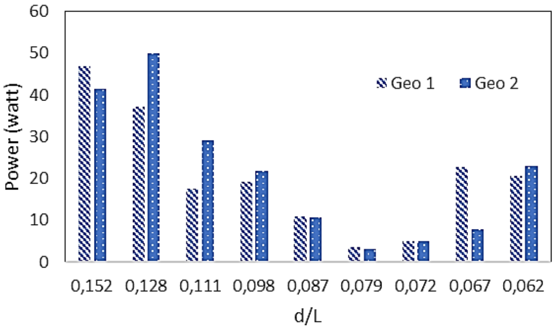

Fig. 12: Comparation of L-OWC Power Generated between Geo 1 and Geo 2

4. Conclusion

This study investigates the performance of L-shaped Oscillating Water Column (L-OWC) chambers through a series of wave flume experiments, focusing on the relationship between water surface oscillation (fse), pneumatic pressure, and airflow velocity. The results confirm that water surface oscillation drives air pressure changes, which directly influence airflow velocity within the turbine duct. Decompression consistently produces higher airflow velocities than compression, suggesting that both Geo 1 and Geo 2 are more efficient during air intake phases.

Air pressure shows a strong correlation with water level oscillations, with Geo 1 generally producing higher pressures than Geo 2, except at a specific wave period (Tin = 2.37 s) where Geo 2 performs better. Across both geometries, decompression airflow velocity is significantly higher than compression, confirming the chambers' potential in converting wave energy to pneumatic energy.

The study highlights the resonance behavior of the chambers, where the highest Water Amplification Factor (WAF) is observed at a d/L ratio of approximately 0.128. Geo 1 reaches a peak WAF of 3.06, while Geo 2 achieves a slightly higher value of 3.21. Performance decreases at lower d/L values due to insufficient water depth and reduced energy input. Power analysis shows that Geo 1 performs better at higher d/L ratios (0.152 and 0.098), while Geo 2 demonstrates better adaptability under moderate wave conditions (d/L ≈ 0.128–0.111).

These findings emphasize the importance of chamber geometry and resonance tuning in maximizing L-OWC energy conversion performance. It is shown by the power output from Geo 2 (49.99 W) slightly bigger than Geo 1 (46.91 W). The performance of Geo 1 and Geo 2 varies with wave period, indicating that each geometry has advantages under specific wave conditions. This underlines the need to optimize a chamber design that suits the dominant wave characteristics of the intended site.

Acknowledgements

This research was supported by funding from the Renewable Energy Program House - OREM of the National Research and Innovation Agency (BRIN) under the 2024 grant scheme, Grant Number B-12293/III.3/HM.07.00/11/2023 and Institut Teknologi Kalimantan.

Nomenclature

COP	coefficient of performance (–)
c_p	specific heat capacity (J kg^{-1} K^{-1})
P	power (W)
$\dot{E}$	exergy rate (W)
h	specific enthalpy (J kg^{-1})
s_0	specific enthalpy of the dead state (J kg^{-1} K^{-1})

Greek symbols

δ	exergy defect (–)
η	efficiency (–)

Subscripts

2nd	Second Law
Carnot	Carnot
Dis	discharge
e	exit

References

1) D. Kassymbekov, and D. Aitkul, “Economic aspects of the benefits of renewable energy considered in the legal framework in different countries,” Evergreen, 11 (2) 576–585 (2024). doi:10.5109/7183311.
2) B. Ganguly, T. Nag, and D. Guha, “P2P prosumer networks: a model for electricity trading,” Evergreen, 11 (3) 1493–1497 (2024). doi:10.5109/7236806.
3) R.A. Jessam, “Experimental study of wind turbine power generation utilizing discharged air of air conditioner blower,” Evergreen, 9 (4) 1103–1109 (2022). doi:10.5109/6625722.
4) A.F. d. O. Falcão, “Wave energy utilization: a review of the technologies,” Renew. Sustain. Energy Rev., 14 (3) 899–918 (2010). doi:10.1016/j.rser.2009.11.003.
5) A.A.M. Rodríguez, J.M.B. Ilzarbe, R.S. Casarín, and U.I. Ereño, “The influence of the chamber configuration on the hydrodynamic efficiency of oscillating water column devices,” J. Mar. Sci. Eng., 8 (10) 1–27 (2020). doi:10.3390/jmse8100751.
6) C.-C. LIN, Y.-C. CHOW, and D.T. NGUYEN, “Geometrical design of the l-shaped oscillating water column using artificial neural network,” Proc. Eur. Wave Tidal Energy Conf., 15 (2023). doi:10.36688/ewtec-2023-555.
7) T. Vyzikas, S. Deshoulières, M. Barton, O. Giroux, D. Greaves, and D. Simmonds, “Experimental investigation of different geometries of fixed oscillating water column devices,” Renew. Energy, 104 248–258 (2017). doi:10.1016/j.renene.2016.11.061.
8) D.G. Dorrell, M.F. Hsieh, and C.C. Lin, “A multichamber oscillating water column using cascaded savonius turbines,” IEEE Trans. Ind. Appl., 46 (6) 2372–2380 (2010). doi:10.1109/TIA.2010.2072979.
9) I. López, R. Carballo, D.M. Fouz, and G. Iglesias, “Design selection and geometry in owc wave energy converters for performance,” Energies, 14 (6) 1–18 (2021). doi:10.3390/en14061707.
10) A.S.D. Marta, Deendarlianto, W. Kongko, Aprijanto, A.T. Rohman, A. Wibowo, and I.Y. Ikhsanudin, “The influence of wave characteristics, tides, and installation conditions of l-shaped owc wave energy converter on energy absorption capability,” Evergr. Jt. J. Nov. Carbon Resour. Sci. Green Asia Strateg., 11 (03) 2607–2617 (2024). doi:https://doi.org/10.5109/7236900.
11) E. Supriyanto, A. Taufiqur, A. Iman, I. Yahya, A. Wibowo, M. Taufiq, A. Musthofa, R. Teguh, M. Penta, A. Dwiputra, Deendarlianto, and A.S.D. Marta, “Results in engineering experimental study of flow characteristics in hydrodynamic and aerodynamic l-shaped and u-shaped oscillating water column chambers,” 25 (December 2024) 1–11 (2025). doi:10.1016/j.rineng.2024.103762.
12) K. Rezanejad, A. Souto-Iglesias, and C. Guedes Soares, “Experimental investigation on the hydrodynamic performance of an l-shaped duct oscillating water column wave energy converter,” Ocean Eng., 173 (November 2017) 388–398 (2019). doi:10.1016/j.oceaneng.2019.01.009.
13) N.P. Juan, V.N. Valdecantos, M.D. Esteban, and J.S.L. Gutiérrez, “Review of the influence of oceanographic and geometric parameters on oscillating water columns,” J. Mar. Sci. Eng., 10 (2) (2022). doi:10.3390/jmse10020226.
14) A.S.D. Marta, Deendarlianto, W. Kongko, Indarto, Fauzun, and A.T. Rohman, “The influence of wave height and period on airflow velocity and differential pressure in l-shaped oscillating water column (l-owc) chamber for wave energy converter (wec),” Asia-Pacific J. Sci. Technol., 29 (6) 5(13) (2024). doi:10.14456/apst.2024.90.
15) H. Khoirunnisa, W. Kongko, A.S.D. Marta, T.B. Pratomo, A. Nurwijayanti, S. Husrin, Benazir, F.M.G. Putra, D. Ariyanto, and K.S. Wardani, “Physical modelling scenarios of tsunami wave attenuation induced by variation of mangrove protection width and sea dike,” Evergreen, 11 (3) 2742–2754 (2024). doi:10.5109/7236913.
16) I. Magdalena, H.Q. Rif’atin, W. Kongko, A.S.D. Marta, H. Khoirunnisa, A. Nurwijayanti, and M. Farid, “Aceh’s tsunami wave evolution and its interaction with hybrid protection structure,” Phys. Fluids, 36 (2) (2024). doi:10.1063/5.0185672.
17) L. Gurnari, P. G.F.Filianoti, and S. M.Camporeale, “Fluid dynamics inside a u-shaped oscillating water column (owc): 1d vs. 2d cfd model,” Renew. Energy, 193 687–705 (2022). doi:10.1016/j.renene.2022.05.025.
18) A.S.D. Marta, Deendarlianto, Indarto, Sarjiya, S.

Kamal, and E. Winata, “Performance of OWC-type wave power plants in the seas of Sumbawa Island , Indonesia,” in: 2024 Int. Conf. Technol. Policy Energy Electr. Power, IEEE, 2024: pp. 1–6. doi:10.1109/ICT-PEP63827.2024.10733542.

19) D.C. Istiyanto, E. Cholishoh, C. Murtiaji, A.B. Widagdo, C.I. Sukmana, A. Hamid, E.A. Wiguna, A.S.D. Marta, J. Setiawan, and B. Santosa, “Laboratory physical modeling of rakuna iv armor block stability and overtopping discharge of patimban port’s rubble mound breakwater,” IOP Conf. Ser. Earth Environ. Sci., 832 (1) (2021). doi:10.1088/1755-1315/832/1/012061.

20) G. Wolters, M. Van Gent, W. Allsop, L. Hamm, and D. Mühlestein, “HYDRALAB iii: guidelines for physical model testing of rubble mound breakwaters,” Coasts, Mar. Struct. Break. Adapt. to Chang. - Proc. 9th Int. Conf., 2 (December 2013) 659–670 (2010). doi:10.1680/cmsb.41318.0062.

21) A. Pecher, and J. Kofoed, “Ocean Wave Energy Book,” 2017.

22) S. John Ashlin, S.A. Sannasiraj, and V. Sundar, “Wave forces on an oscillating water column device,” Procedia Eng., 116 (1) 1019–1026 (2015). doi:10.1016/j.proeng.2015.08.336.

23) R.M. Sorensen, “Basic Coastal Engineering,” 2006. http://scioteca.caf.com/bitstream/handle/123456789/1091/RED2017-Eng-8ene.pdf?sequence=12&isAllowed=y%0Ahttp://dx.doi.org/10.1016/j.regsciurbeco.2008.06.005%0Ahttps://www.researchgate.net/publication/305320484_SISTEM_PEMBETUNGAN_TERPUSAT_STRATEGI_MELESTARI.

24) J.A. López-Leyva, C. Barrera-Silva, L.F. Sarmiento-Leyva, and M.F. González-Romero, “Simulation and characteristics analysis of on-shore owc system proposal as distributed generation resource considering the irregular wave interaction,” Electron., 10 (7) (2021). doi:10.3390/electronics10070773.

25) M.M. Samak, H. Elgamal, and A.M. Nagib Elmekawy, “The contribution of l-shaped front wall in the improvement of the oscillating water column wave energy converter performance,” Energy, 226 120421 (2021). doi:10.1016/j.energy.2021.120421.

26) E. Mansard, and E. Funke, “Reflection analysis of non-linear regular waves,” Natl. Res. Counc. Canada, TR-HY-011 (NRC No. 25144) 280–287 (1977).

27) L.E. Frostick, S.J. McLelland, T.G. Mercer, J. Kirkegaard, G. Wolters, J. Sutherland, R. Soulsby, L. Frostick, S. McLelland, T. Mercer, and H. Gerritsen, “Users Guide to Physical Modelling and Experimentation: Experience of the HYDRALAB Network,” 2011. doi:10.1201/b11335.

28) K. Ram, M. Faizal, M.R. Ahmed, and Y.H. Lee, “Experimental studies on the flow characteristics in an oscillating water column device,” J. Mech. Sci. Technol., 24 (10) 2043–2050 (2010). doi:10.1007/s12206-010-0621-z.

29) J.P. Thavamani, “Bernoulli equation in fluid flow,” Int. J. Curr. Res., 8 (10) 59–61 (2016). http://www.journalcra.com.

30) ISO/CASCO, “INTERNATIONAL standard iso / iec competence of testing and calibration,” Int. Organ. Stand., 2017 1–38 (2017). https://www.iso.org/fr/standard/39883.html.

31) J. Hodges, J. Henderson, L. Ruedy, M. Soede, J. Weber, P. Ruiz-Minguela, H. Jeffrey, E.B. Bannon, M. Holland, R. Maciver, D. Hume, J.L. Villate, and T. Ramsey, “An international evaluation and guidance framework for ocean energy technology,” (August) 68 (2021).

32) A.A. Medina Rodríguez, G. Posada Vanegas, B.E. Vega Serratos, I. Oderiz Martinez, E. Mendoza, J.M. Blanco Ilzarbe, V. Sundar, and R. Silva, “The hydrodynamic performance of a shore-based oscillating water column device under random wave conditions,” Ocean Eng., 269 (August 2022) 113573 (2023). doi:10.1016/j.oceaneng.2022.113573.

33) J.F.M. Gadelho, K. Rezanejad, C. Guedes Soares, J.A. Santos, G. Anastas, and C.J.E.M. Fortes, “Experimental study of an onshore dual chamber oscillating water column device,” Ocean Eng., 300 (May 2023) 117240 (2024). doi:10.1016/j.oceaneng.2024.117240.

34) D.Z. Ning, R.Q. Wang, Q.P. Zou, and B. Teng, “An experimental investigation of hydrodynamics of a fixed owc wave energy converter,” Appl. Energy, 168 636–648 (2016). doi:10.1016/j.apenergy.2016.01.107.

35) Y. Eskİ, “A laboratory study on the design and performance evaluation of pitot-tube a laboratory study on the design and performance evaluation of pitot-tube,” J. Innov. Sci. Eng., 7(2) (October) 122–132 (2023). doi:10.38088/jise.1233700.